Nonlinear Dyn (2025) 113:30497–30513
https://doi.org/10.1007/s11071-025-11230-z

RESEARCH

Vibration control via finite and semi-infinite vibration attenuation regions in the chain of mass-in-mass units: from theory to experiments

Ivana Kovacic · Ljiljana Teofanov · Rui Zhu · Xiao Wang · Jianlei Zhao

Received: 29 September 2024 / Accepted: 8 April 2025 / Published online: 11 May 2025

Abstract This study deals with a longitudinally excited chain of external linear oscillators, enhanced with internal linear oscillators. The undamped case is considered first as a benchmark, and then a viscously damped chain is examined. Qualitatively different vibration attenuation regions are identified, including the cases of no attenuation region, a finite and semi-infinite attenuation region, which represents a new result for this type of chain of interest for vibration control. The influence of the number of unit cells, the mass and the damping ratio on their appearance is examined thoroughly and illustrated in the form of novel and original 2D and 3D behavioural maps, which can be used as a design criterion for metastructures, but also for other systems modelled as this type of chains. The nonlinear boundary between the finite and semi-infinite vibration region involving the non-dimensional damping coefficient and the number of units is determined for the first time. Besides, the nonlinear change of the critical non-dimensional damping ratio, which assures the appearance of the semi-infinite vibration attenuation region in the system response, with the non-dimensional total mass, is also innovatively obtained. The theoretical identification of three distinct regions of vibration attenuation is experimentally validated through an original damping control method utilizing an air track and an air pump with a variable power output capability.

Keywords Chain · Oscillators · Vibration attenuation regions · Behavioural mapping

I. Kovacic (✉)
Faculty of Technical Sciences, Centre of Excellence for Vibro-Acoustic Systems and Signal Processing CEVAS, University of Novi Sad, Novi Sad, Serbia
e-mail: ivanakov@uns.ac.rs

L. Teofanov
Faculty of Technical Sciences, University of Novi Sad, Novi Sad, Serbia

R. Zhu · X. Wang · J. Zhao
School of Aerospace Engineering, Beijing Institute of Technology, University of Novi Sad, Beijing 100081, China

1 Introduction

Chains are widely known as representing a sequence of items of the same type forming a line, a set of connected or related things, or as something that confines, restrains or secures [1]. Chains appear in nature, everyday life as well as in science and engineering. In nature, one can recognize, chains of mountains and islands, or food chains. In everyday life, there are chains of events, supply chains, chains of stores, etc. [2]. There is also a chain of action and reaction, and one of the most powerful examples of the latter is nuclear fission. In structural engineering, chains are used either for lifting and securing, or for transferring power in machines. Besides this, the chain

is a unit of length equal to 66 feet [3], used in both the US customary and Imperial unit systems; it is the basic unit for measuring distances in fire-control work.

Oscillatory chains appear as a distinctive model of various biological, physical, or engineering systems [4, 5]. There have been two types of co-axial oscillatory chains that can be considered as prominent and pivotal during the previous century or so for the developments in science and engineering, especially related to mechanics and solid-state physics. Chronologically speaking, the first one is related to the name and work of den Hartog [6] and the second one to the names of Fermi, Pasta and Ulam [7].

Den Hartog's work involves the chain in which the main (host) oscillatory structure is enhanced with the auxiliary oscillator, playing the role of the vibration absorber (tuned mass damper) that is tuned to the structural and excitation resonance frequency so that it reduces the resonance response of the host structure [6]. This theoretical foundation has resulted in the advancements in plethora of optimizing approaches of various vibration suppression devices [8–11], which are widely used nowadays in structural, automotive and aerospace engineering. Some of the respective examples include the world's tallest skyscrapers (e.g. Taipei 101 tower in Taipei City and Burj al-Arab in Dubai), cars produced by the world's most famous automobile manufacturers (e.g. Renault F1 car, Citroën 2CV, BMW 320D) as well as space vehicles (e.g. NASA's crew launch vehicle called Ares).

On the other hand, Fermi, Pasta and Ulam's oscillatory chain [7] stems from the original idea of Fermi to simulate the one-dimensional analogue of atoms in a crystal as a long chain of particles linked by springs with weak nonlinear correction either quadratic or cubic one to its linear stiffness characteristic. This system behaved in a surprising way: contrary to the predictions of statistical mechanics when the number of particles is going to infinity, the energy equipartition state was not reached, and energy was periodically returning to the initially excited mode. This highly remarkable result, known as the FPU paradox, shows that nonlinearity is not enough to guarantee the equipartition of energy, which marked the beginning of nonlinear physics, the theories of solitons and chaos, and also the age of computer simulations of scientific problems.

The idea about the use of chain of oscillators has also recently been brought to bear in metamaterials and metastructures for controlling their low-frequency vibrations [12, 13], with the horizons being opened by the Science paper [14]. Given the fact that our work addresses their utilization for passive longitudinal vibration control, the overview of the state-of-the-art is given related to the findings about attenuation zones (bandgaps) within which the zero or low transmissibility is achieved. In [15], a slender beam with periodically attached oscillators was studied. The maximum of attenuation was observed at the resonant frequency of the oscillators as inversely proportional to the mass ratio of the mass of the oscillator and the mass of the beam per period and proportional to the stiffness ratio of the oscillator and the equivalent stiffness of the beam per period. It was demonstrated in [16] that a metamaterial containing multiple microstructures with a spectrum of local resonance frequencies enables the system to have a significantly reduced magnitude of the waves generated by the dynamic source. In [17], the same mechanical model was studied, showing that the effective mass density is frequency-dependent and may become negative near the resonance frequency of the internal mass. In [18], a uniform rod with periodically attached multi-degree-of-freedom spring–mass oscillators were examined. The bandgap formation mechanisms are explained, and expression derived for the band edge frequencies. In [19], the case of periodically attached multi-degree-of-freedom local oscillators was investigated. Experiments showed that low damping vibration responses exist before the bandgap and high damping vibration responses appear after the bandgap. The study [20] demonstrated that a working principle of metamaterial-based elastic wave absorber corresponds to the concept of conventional den Hartog vibration absorbers [6]. This concept was extended to design a broadband absorber that works well for elastic waves of any wavelengths, including those shorter than the unit cell's length. In [21], the metamaterial whose stopband commences at 0 Hz is presented. The dominant effect of mass and stiffness of discrete units on the transmissibility is found to be dominant with respect to the effect of damping on the stopband was found to be relatively small when compared with the effects of mass and stiffness. In [22], the concept of integrated internal oscillators in a longitudinally excited metastructure extended presented and then

analysed in detail in [23]. The latter study compared a metastructure with vibration absorbers to a structure of equal mass with no absorbers. Numerical simulations showed that the distributed absorbers should be designed such that their natural frequencies span a range of frequencies. This concept was further considered in [24], where a minimal number of absorbers is obtained, yielding the proper tuning between the metastructure and internal oscillators and resulting in the desirable vibration attenuation around the first resonance.

The current study aims to contribute to the fundamental knowledge and demonstrate its original applications by linking two previously described prominent models of den Hartog [6] and Fermi, Pasta and Ulam [7] in an original way to determine its benefits for vibration suppression in metamaterials and metastructures modelled as chains of oscillators. The links with den Hartog's work will be established in a way that the same type of tuning will be defined: internal oscillators will have the natural frequency adjusted to the natural frequency of the external (main) oscillators. The links with Fermi, Pasta and Ulam's work assumes the investigations of the influence of the increasing number of oscillatory units to the response of the chain. In addition, this study also contains the original contribution of the influence of damping, revealing qualitatively different outcomes in terms of a finite and semi-infinite vibration attenuation region, which are seen to be opening horizons for practical applications, not only for metastructures, but also for systems from other fields modelled as the same type of chains of oscillators.

2 Chain of mass-in-mass units: den Hartog's tuning

A mechanical model considered corresponds to a chain of repetitive mass-in-mass units (Fig. 1). The external (host, main) masses m that stand for the basic structure are attached mutually via linear springs of stiffness k. The internal oscillators are uniform, i.e. they are all equal: each has the mass m_1 and it is attached to the external mass via linear spring of stiffness k_1. The structure is exposed to the base excitation $Z_0\cos\Omega t$ and it exhibits longitudinal vibrations. The generalized coordinates for the ith unit are labelled, respectively, by the absolute coordinates x_i and y_i, where $i = 1, \ldots, n$.

2.1 Undamped model

The undamped case is considered for the sake of subsequent comparison with the damped case. The equations of motion for the ith unit can be written down as

$$\begin{aligned} &m\ddot{x}_i + k(2x_i - x_{i-1} - x_{i+1}) - k_1(y_i - x_i) = 0 \\ &m_1\ddot{y}_1 + k_1(y_i - x_i) = 0. \end{aligned} \tag{1}$$

The natural frequencies of each external and internal oscillator are respectively given by $\omega_0 = \sqrt{k/m}$ and $\omega_1 = \sqrt{k_1/m_1}$. Besides these substitutions, the following non-dimensional parameters are introduced: the non-dimensional frequency as the ratio of the excitation frequency and the natural frequency of the external oscillator $\psi = \Omega/\omega_0$; the non-dimensional stiffness as the ratio of the stiffness coefficient of the internal and external oscillator $\kappa = k_1/k$; the non-dimensional mass as the ratio of the mass of the internal and external oscillator $\mu = m_1/m$.

Given the fact that the system considered is linear, the solutions for motion can be taken in the form proportional to the excitation [25]. Then, the set of resulting equations of motion is solved analytically in *Wolfram Mathematica* for each fixed value of n with a view to determining the amplitude of the last main mass A_n, i.e. the top of the metastructure, as labelled in Fig. 1. Note that for the first unit, one needs to include the base excitation into the corresponding equation of motion.

The way how the nondimensional amplitude A_n/Z_0 changes with the nondimensional frequency ψ, is shown in Fig. 2. The stopband is also indicated. This region appears between the left and right resonance values ψ_L and ψ_R, which are placed here at the corresponding vertical asymptotes.

Of further interest is to determine how the width of this stopband Δw changes with the number of units n for the reduction of A_n being 60 dB. These results are obtained numerically. Given the fact that the model is conservative, this high reduction assures that the amplitude will be as close to zero as possible. The nondimensional mass ratio is assumed to be $\mu = 1$ (note that this value will be changed later on), while the nondimensional stiffness ratio is also taken to be

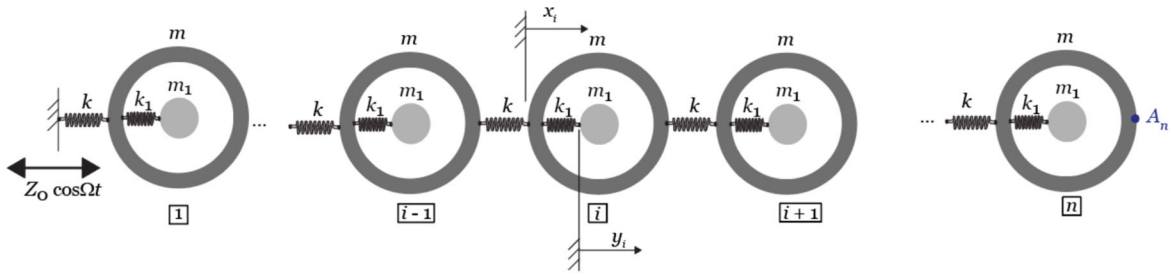

Fig. 1 Mechanical model under consideration with mass-in-mass units

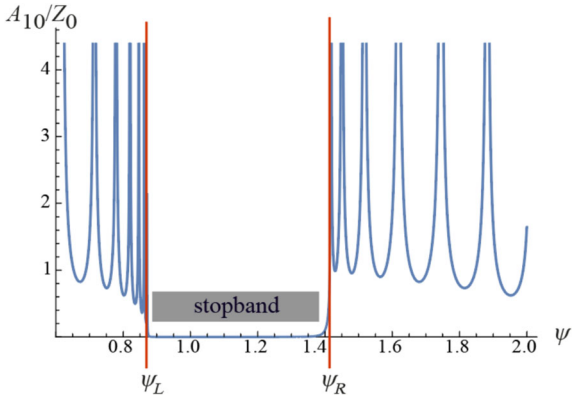

Fig. 2 Frequency–response function for the top mass in the undamped chain with the stopband labelled

$\kappa = 1$ for the whole study as well as that the nondimensional mass ratio takes the same value. It should also be noted that this case corresponds to the classical den Hartog's tuning, $m_1/m = k_1/k = 1$, which implies that the natural frequencies of the internal and external oscillators are tuned to each other $\omega_0 = \omega_1$. The change of Δw with n ranging from 0 to 100 is presented in Fig. 3. The enlargement of this figure for a smaller number of internal masses until 10 is given on the right part of Fig. 3. It can be concluded that for a smaller number of these masses, the width of the stopband is very small. As this number increases, until appr. 10, the width increases more rapidly, and then after app. 30 of them, its change becomes negligible, i.e., the saturation phenomenon appears. This implies that adding more units will not widen the attenuation region.

The way how the width of the stopband Δw changes with the number of units n for various mass ratios μ is plotted in Fig. 4a. It is seen that as μ decreases from unity, this width narrows down as well. However, this change is qualitatively the same as the one shown in Fig. 3, meaning that as the number of units gets larger, the phenomenon of saturation appears and there is no further widening of the stopband.

The relocations of the vertical asymptotes ψ_L and ψ_R with the number of units n for various mass ratios μ is presented in Fig. 4b. As this ratio becomes smaller, both ψ_L and ψ_R approach the value $\psi = 1$, considerably narrowing down the width of the stopband.

2.2 Damped model

To take into account the influence of damping, linear viscous dampers are introduced into the mechanical model of a metastructure as shown in Fig. 5 they are set in parallel with the springs that connect units mutually as well in parallel with the springs that connect each internal mass with the external one. The damping coefficient of the former is labelled by b, and the latter by b_1.

The equations of motion for the ith unit can now be extended to

$$\begin{aligned} m\ddot{x}_i + b(2\dot{x}_i - \dot{x}_{i-1} - \dot{x}_{i+1}) + k(2x_i - x_{i-1} - x_{i+1}) \\ -b_1(\dot{y}_i - \dot{x}_i) - k_1(y_i - x_i) = 0 \\ m_1\ddot{y}_i + b_1(\dot{y}_i - \dot{x}_i) + k_1(y_i - x_i) = 0. \end{aligned} \tag{2}$$

As in the previous section, the non-dimensional frequency ψ, the non-dimensional stiffness κ, and the non-dimensional mass μ are introduced. In addition, the non-dimensional damping coefficient is defined as $\rho = b_1/b$, while the non-dimensional damping ratio is taken as $\zeta = b/(2m\omega_0)$.

The system of equations of motion is again solved analytically in *Wolfram Mathematica* for each fixed value of n to obtain A_n. Since A_n involves rational functions with polynomials of degree 8n, certain algebraic manipulations are required to make this term

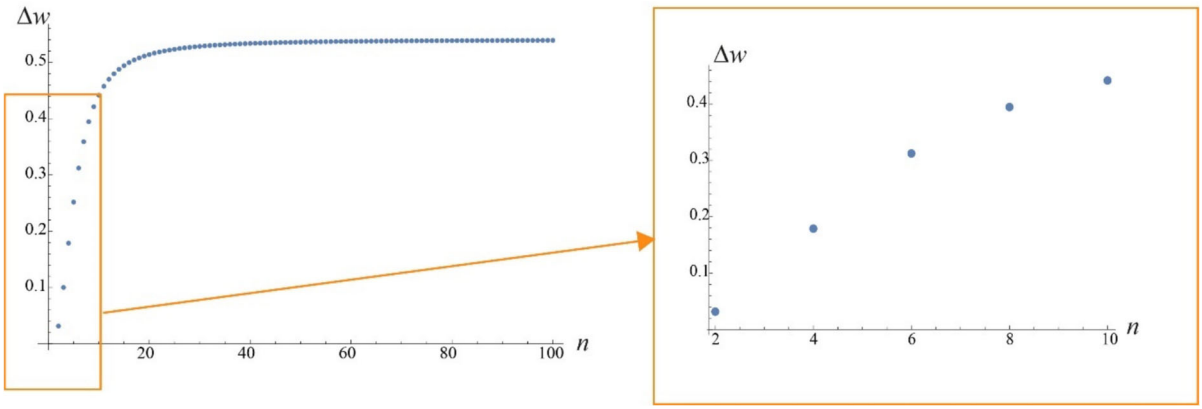

Fig. 3 Change of the width of the stopband with the number of units n; The enlarged part of the graph on the righthand side is shown for a smaller number of units n

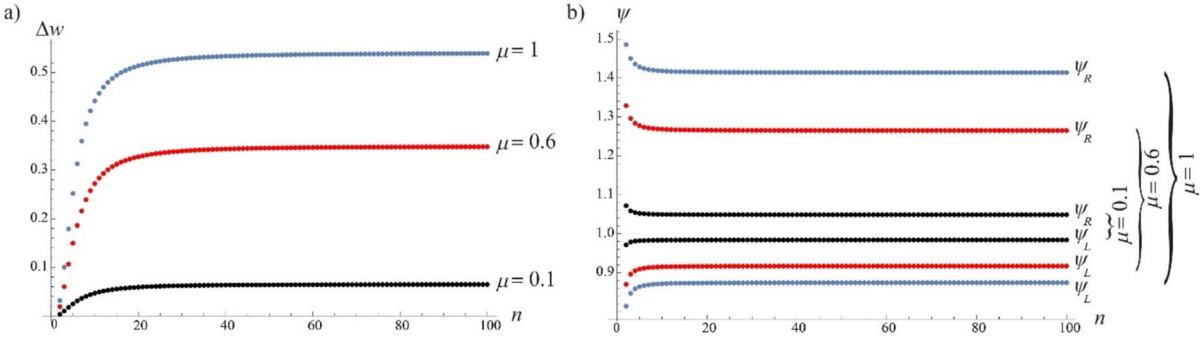

Fig. 4 **a** Change of the width of the stopband Δw with the number of units n for various mass ratios μ; **b** Relocation of the vertical asymptotes ψ_L and ψ_R with the number of units n for various mass ratios μ

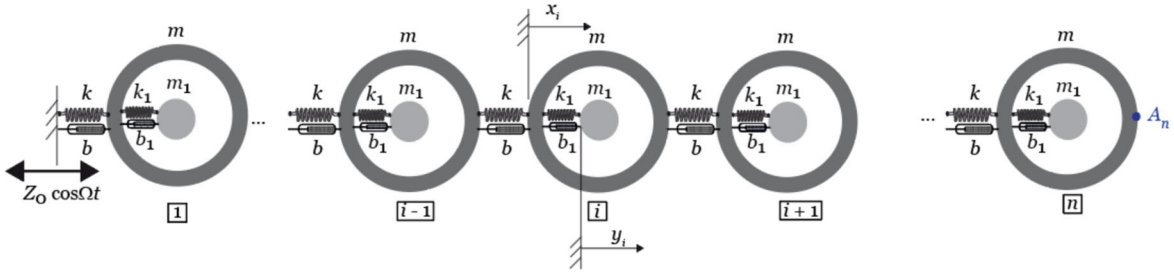

Fig. 5 Mechanical model of under consideration with mass-in-mass units

suitable for further use in numerical algorithms. Given the calculation requirement, all calculations for $n > 40$ are done with High Performance Computing, during which a server AMD EPYC 7282 processor with 16 cores, 32 threads, and 128GB RAM was used. The reduction of the amplitude of the top mass A_n with respect to the excitation amplitude is set to correspond to 20 dB. Typical and qualitatively different illustrative forms of its frequency–response function are presented in Fig. 6. The one presented in Fig. 6a is when such reduction is not achieved along the frequency region considered, i.e. up to $\psi = 2$. The next one shown in Fig. 6b is similar to the one from Fig. 2 with respect to the existence of a bandgap

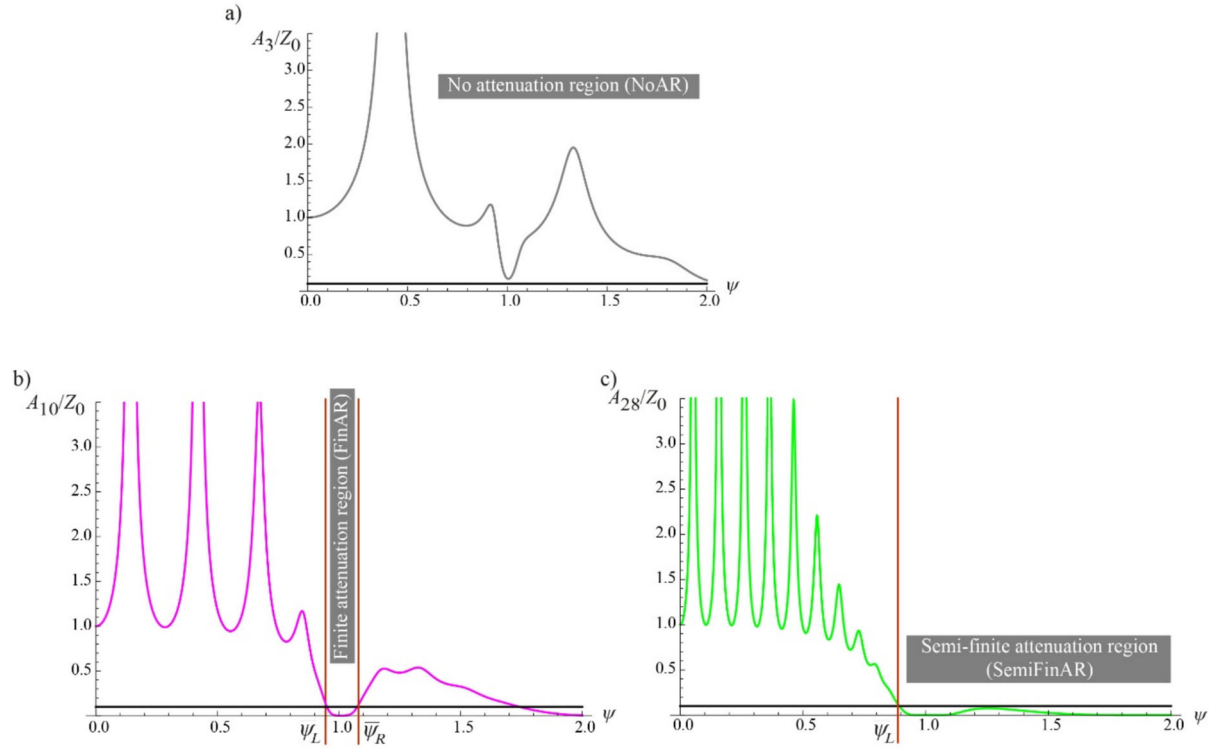

Fig. 6 Qualitatively different frequency–response functions for the top mass in the damped metastructure obtained for $\mu = \rho = 0.1$, $\zeta = 0.04$ and the desired vibration attenuation of 20 dB: **a** NoAR case (the graph is obtained for $n = 3$); **b** FinAR case (the graph is obtained for $n = 10$); **c** SemiFinAR case (the graph is obtained for $n = 28$)

bounded on both sides, i.e. it is limited by $\overline{\Psi}_{\mathrm{L}}$ and $\overline{\Psi}_{\mathrm{R}}$. In the case presented in Fig. 6c, the attenuation appears in a frequency region bounded on the left-hand side only by $\overline{\Psi}_{\mathrm{L}}$, which means that it is of a semi-infinite width. This is similar to a vibration isolation region that appears in a linear one-degree of freedom externally excited system [26]. The first case will be referred subsequently as the NoAR (no attenuation region), the second case as FinAR (finite attenuation region), and the third one as SemiFinAR (semi-infinite attenuation region), and as far as the authors are aware, this distinction and characterization appears for the first time in the context of vibration control of the chains under consideration.

To examine the influence of the number of units n on the appearance of FinAR and SemiFinAR, it is again assumed that $\mu = \rho = \kappa = 1$. Figure 7 shows the width of the attenuation region changes when the non-dimensional damping ratio is taken first to be $\zeta = 0.01$ (magenta dots). The curve for the undamped system from Fig. 3a is also plotted (blue dots) to emphasize the qualitative and quantitative changes. It is seen that the width is finite only until a certain number of the masses (app. 40 of them), and then the case of the semi-infinite one occurs as the magenta curve does not appear anymore. So, unlike the undamped case when the width becomes constant after app. 10 masses, in the damped case, the width monotonously increases until a considerably larger number of units and then it turns into SemiFinAR. As also shown in Fig. 7, if ζ takes larger values, the SemiFinAR case appears for a smaller number of units.

The enlargement of these curves for both the undamped and damped case is shown in the right part of Fig. 7. It is seen that for a smaller number of units (until app. 10 of them), the undamped and lightly damped system behave almost the same in this respect as the width of FinAR is equal or almost equal to the undamped case (the magenta and blue dots coincide or are very close to each other).

The way how the width of the attenuation region Δw changes with the number of units n for various

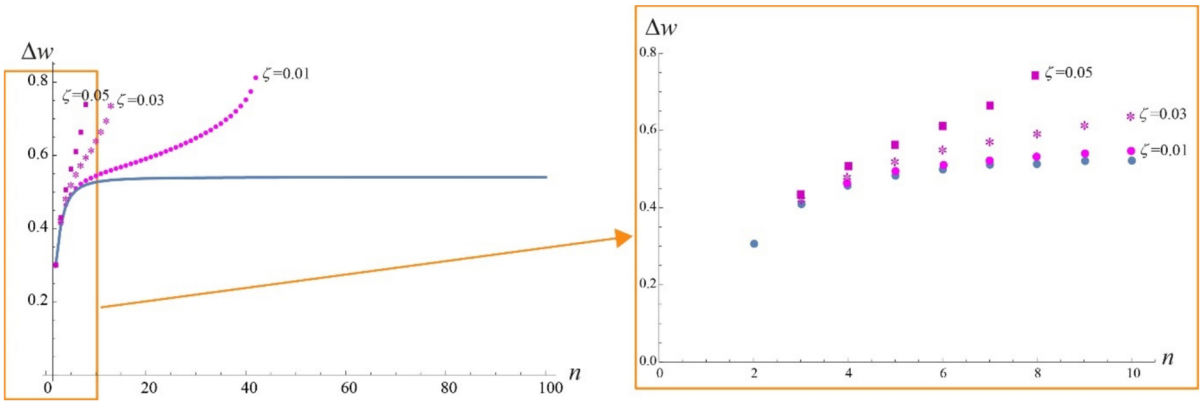

Fig. 7 Change of the width of the attenuation region with the number of units n in the damped chain (magenta dots, asterisks and squares correspond to FinAR) and the undamped one (blue solid line is the repetition of the results from Fig. 3); The enlarged part of the graph on the righthand side is shown for a smaller number of units n

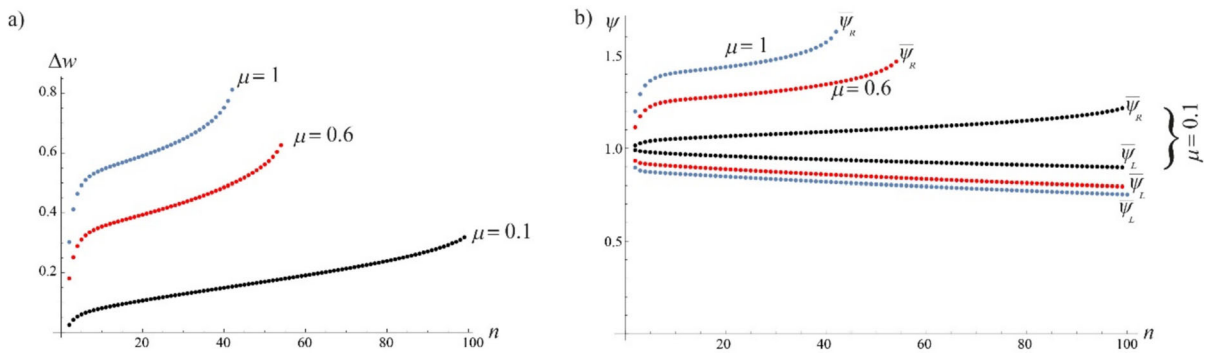

Fig. 8 Change of the width of the stopband Δw with the number of units n for various mass ratios μ; **b** Relocation of the left and right boundaries $\overline{\psi}_R$ and ψ_L with the number of units n for various mass ratios μ

mass ratios μ is plotted in Fig. 8a. It is seen that as μ decreases from unity, this width narrows down, as was the case in the undamped system as well. However, unlike therein, when μ is very small, it does not exist for a smaller number of units. In addition, as μ increases, the SemiFinAR case appears for a smaller number of units.

The relocations of the boundaries of the FinAR with the number of units n is presented in Fig. 8b. The left boundary always exists, and its value decreases with the increase of n, while the right one moves towards higher frequency and then disappears, meaning that the SemiFinAR takes place.

It is of interest now to carry out behavioural mapping, i.e. determine when, depending on the combination of the system parameter, each of three qualitatively different responses from Fig. 6 will take place. Such behavioural maps in 2D are given in Fig. 9 for various values of $\mu = \rho = \kappa$. When these values are small as shown in Fig. 9a for $\mu = \rho = 0.1$, the dominant is the case of FinAR, while SemiFinAR appears for after a certain number of units (app. 20), and then this region widens for larger damping. The case of NoAR exists only for a very small number of units and widens for larger damping. As the value of $\mu = \rho$ increases, this region disappears, while the case of SemiFinAR extends, as seen in Fig. 9b, c. These diagrams can be used for the design of the metastructure, defining the combination of the number of units and damping for a given $\mu = \rho$ that will yield the SemiFinAR response, and, thus, beneficial vibration performance in a wider frequency region.

What is pointed out in Fig. 9 by the black solid line is the boundary between the SemiFinAR and FinAR region. Numerical investigations have shown that this

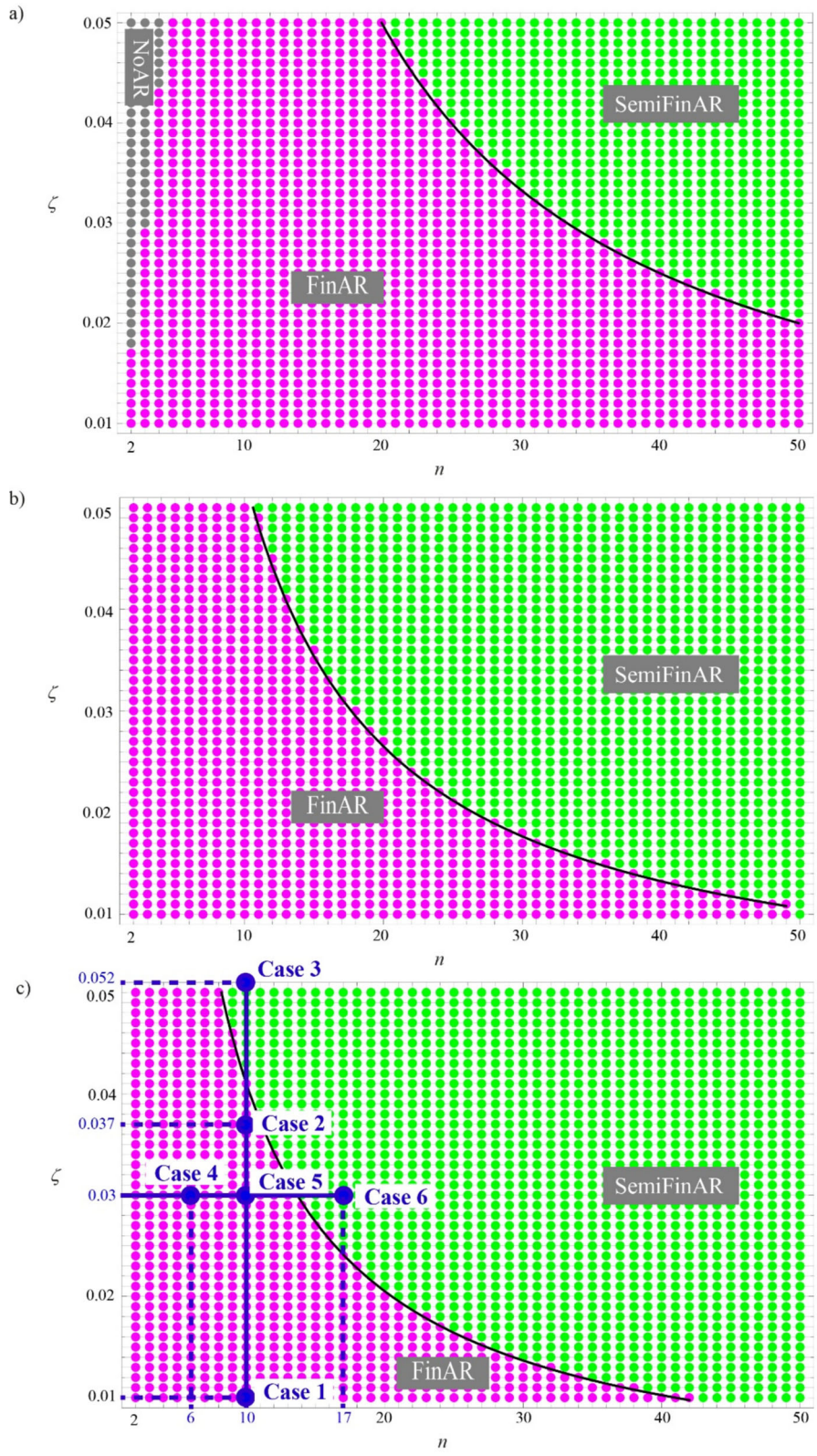

Fig. 9 Behavioural mapping plotted in 2D for various values of $\mu = \rho$: **a** $\mu = \rho = 0.1$; **b** $\mu = \rho = 0.6$; **c** $\mu = \rho = 1$ (Cases 1–6 are discussed in Sect. 3.3 and are associated with the diagrams presented in Figs. 18 and 19)

boundary can be approximately expressed by the equation:

$$\zeta = \frac{K(\mu)}{n}, \tag{3}$$

implying that the non-dimensional damping coefficient and the number of units are inversely proportional with the coefficient $K(\mu)$ that depends on the mass ratio μ, which is a new result. The way how this coefficient changes with μ is presented in Fig. 10. It is seen that the larger the mass ratio, the smaller the coefficient K. It is interesting to note that for the light subunits corresponding to $\mu = 0.1$, one has $K(0.1) = 1$.

In Fig. 11, behavioural mapping is shown for several values of the number of units. As n increases, there is a larger number of combinations of the non-dimensional mass ratio μ and the non-dimensional damping ratio ζ yielding the SemiFinAR response. So, for lighter metastructures, the higher the number of units, the smaller damping is needed to achieve it.

To get deeper insight into the change of distribution of the characteristic regions, the behavioural mapping is created in 3D as dependent on the number of units n, the non-dimensional damping ratio ζ, and the non-dimensional mass ratio μ being equal to the non-dimensional damping coefficient ρ. The presentation is given for more dense values of $\mu = \rho$, and presented in Fig. 12. It is clearly seen how the SemiFinAR case extend with the increase of the parameters shown. It is important to note that there is a threshold of damping for which the SemiFinAR case appears, and it depends on the number of units. This threshold decreases as the number of units increases. The trend how it changes in Figs. 9 and 12, indicates that for very small number of them, the SemiFinAR case might be physically unattainable, as for the range of ζ considered, the NoAR and FinAR can only appear, as seen in Fig. 9.

Figure 13 shows when the SemiFinAR behaviour appears depending on the combination of the non-dimensional total mass being defined by $\mu_T = (m + m_1)n/m = (1 + \mu)n$ and ζ. This diagram can be seen from the point of view of the minimal total mass for a certain non-dimensional damping ratio, which are the cases depicted by the black dots. On the other hand, these combinations of the parameters plotted as the black dots can also be interpreted as the so-called critical ones, since for the fixed μ_T and the higher value of ζ than the one depicted by the black dot, one can assure the appearance of the SemiFinAR behaviour in the system.

For the sake of practical reasons, it is valuable to know how the critical non-dimensional total damping ratio changes with the influence of smaller number of units and, therefore, smaller total mass. Such results from Fig. 13 are presented in Fig. 14 for smaller values of μ_T. In addition, the fitting numerical procedure for a curve imbedding the black dots resulted in the expression:

$$\zeta = \frac{0.86}{\mu_T}. \tag{4}$$

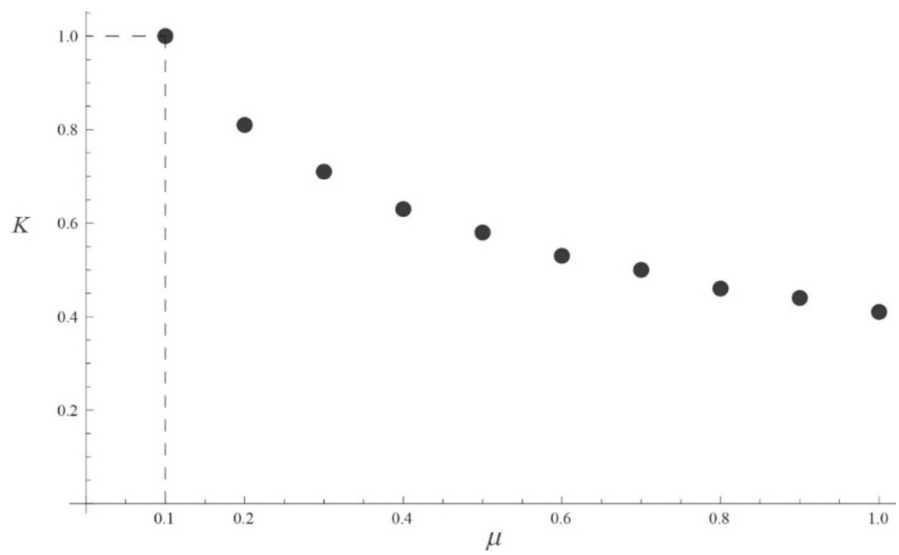

Fig. 10 Change of the coefficient K from Eq. (3) with the mass ratio μ

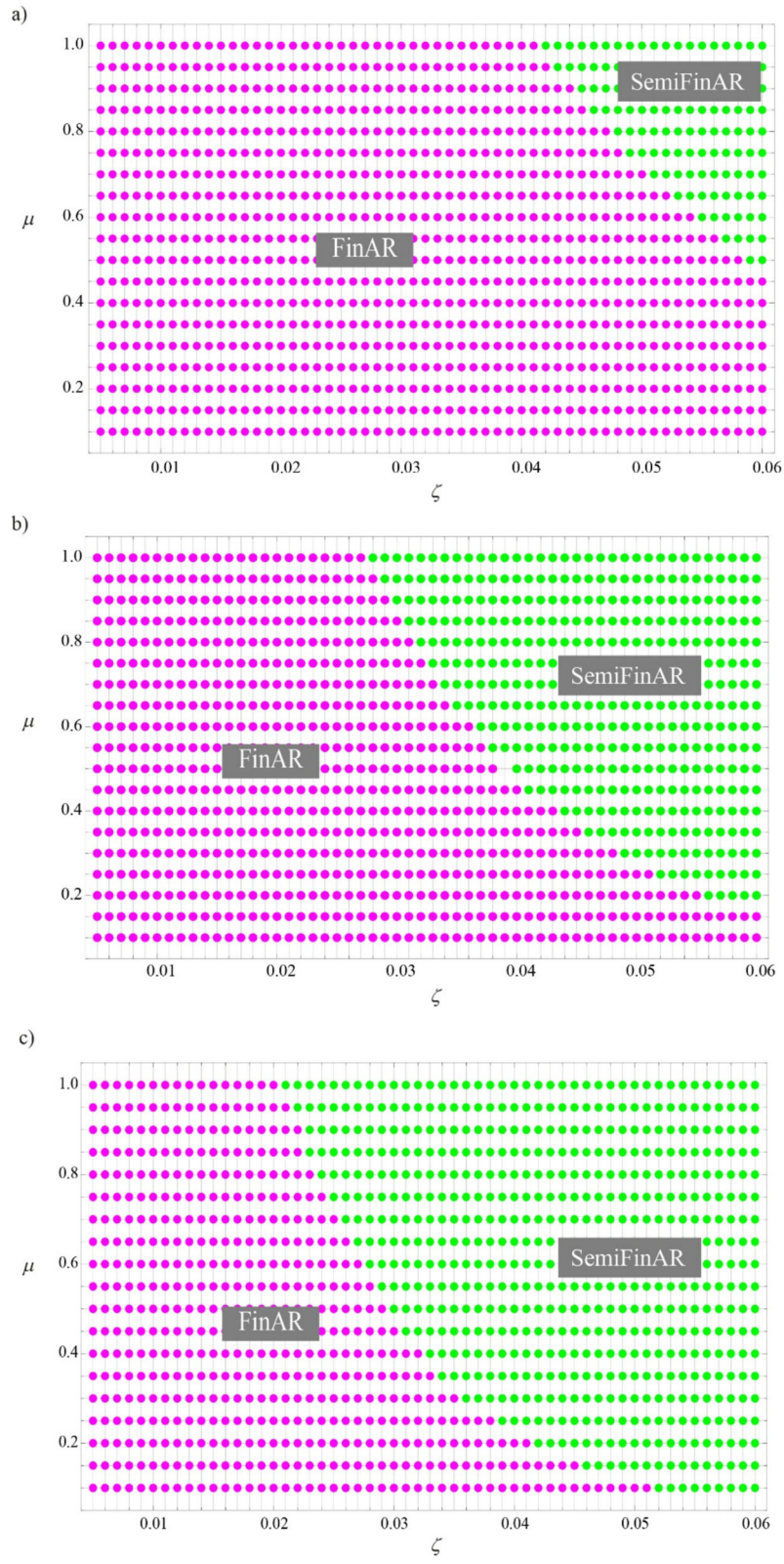

Fig. 11 Behavioural mapping plotted for $\mu = \rho = \kappa$ and various n: **a** $n = 10$; **b** $n = 15$; **c** $n = 20$

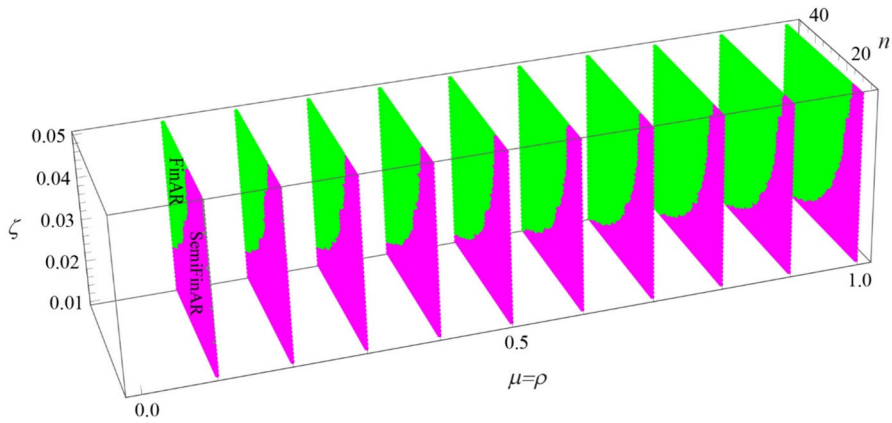

Fig. 12 Behavioural mapping plotted for $\mu = \rho$in 3D presentation for various n and ζ

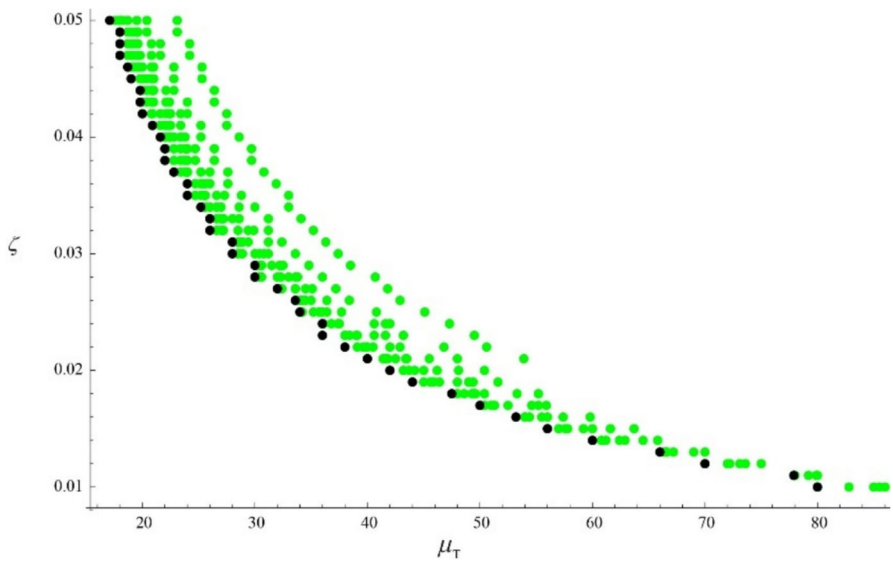

Fig. 13 The appearance of the SemiFinAR case (green dots) for the combination of the total mass μ_T and ζ, where the black dots stand for the minimal total mass needed for a certain (critical) non-dimensional damping ratio

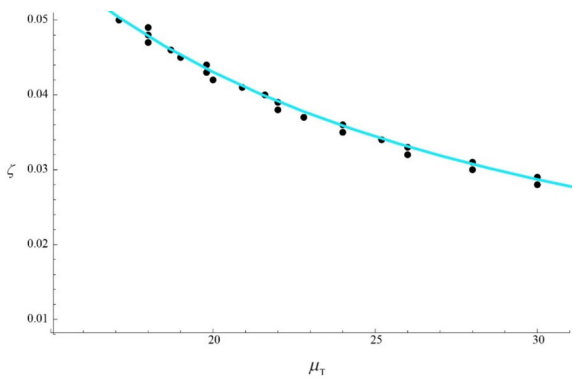

Fig. 14 Critical values of the non-dimensional damping ratio versus the total mass μ_T for a smaller number of units (black dots) and the fitted curve (cyan solid line)

This implies that, in this type of metastructures, there is a conservation law for the critical non-dimensional damping ratio and the minimal total mass needed, meaning that their product is constant and smaller than unity, i.e. $\zeta\mu_T = 0.86$.

3 Validations

3.1 Experimental setup

To provide experimental validation of the previous theoretical findings, a metastructure of $n = 10$ is produced, as shown in Fig. 15a. The external and internal oscillators are 3D printed from polylactic acid (PLA), as shown in the prototype of the unit cell in

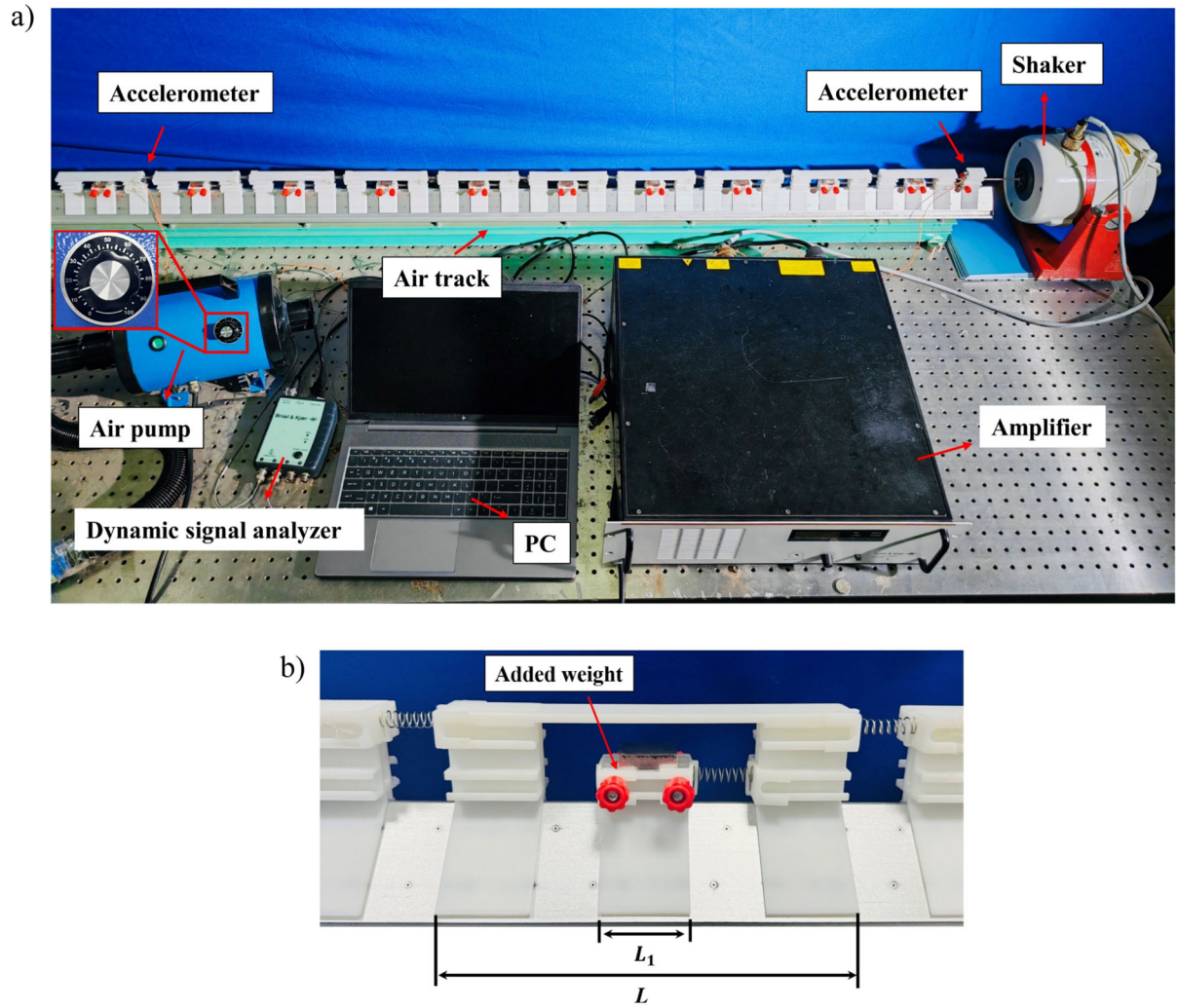

Fig. 15 **a** Experimental set-up of the vibration testing of the metastructure with 10 unit cells; **b** Prototype of the mass-in-mass unit

Fig. 15b, the lengths of the external and internal oscillators are $L = 135\text{mm}$ and $L_1 = 30.3\text{mm}$, respectively. Additional weight is added to the internal oscillator to ensure that the nondimensional mass ratio is $\mu \approx 1$, as considered theoretically in the previous section. Both the external mass m and the internal mass m_1 are approximately 35.3 g, the deviations in mass and mass ratio of the unit cells are both below 1.1%. All the oscillators are connected by the identical springs, each with a stiffness of $k = k_1 = 451.96\text{N/m}$. The deviations in stiffness are within 3.5%; therefore, it can be reasonably assumed that $\kappa \approx 1$, which is consistent with the theoretical considerations.

In the experiment, the metastructure is placed horizontally. To control the damping ratio during the system's motion, a triangular cross-sectional air track was used. The metastructure is positioned on the air track, and its base was designed in a Λ shape to perfectly fit the track. The air track is driven by an air pump, which creates high-pressure airflow through small holes on the track's surface, lifting each unit cell off the track. The air pump has an adjustable power output function to control the damping between the prototype and the air track. One end of the metastructure is excited by a shaker (LDS V406, Brüel & Kjær), while the other end is free. The shaker is powered by a power amplifier (LDS LPA600, Brüel & Kjær), and the excitation signal is a single-frequency sine wave. The response curves from the excitation and the terminal cell are captured as the system's input and

output signals by two accelerometers. The two signals are collected using a dynamic signal analyzer (PHOTON +, Brüel & Kjær) and subsequently processed by a laptop installed with data recorder software. By applying Fourier transform to the two time-domain signals, the input amplitude A_0 and output amplitude A_{10} in the frequency domain are obtained.

3.2 Damping identification experiment

By varying the output power of the air pump, the damping ratio of the external and internal oscillators can be adjusted within a certain range. At different pump power levels, the responses of the free decay oscillation are recorded using accelerometers, and the damping ratio of the system is measured using the logarithmic decrement method. The decay curve of the acceleration can be fitted to an exponential function $A_c = \overline{A}e^{-\zeta\omega_0 t}$, where A_c is the varied acceleration amplitude, $\overline{A}$ is a constant, and ω_0 denotes the undamped natural frequency.

The output power range of the air pump is 0–100, as shown in the enlarged view of Fig. 15 (with 100 being the maximum power). Enhancing the power can increase the airflow rate, thereby further reducing the system's damping. Figures 16a and b show the decay curves of the external oscillator at powers of 5 and 100, respectively. Fitting these curves yields damping ratios of 0.055 and 0.0057.

Figure 17 shows the damping ratios of the external and internal oscillators at six different output power. It can be observed that with the increase of pump power, the damping ratio is gradually smaller and tends to be equal. For the external oscillator, the front and rear contact surfaces jointly affect the damping ratio. At lower powers, the differences in the contact conditions between the two surfaces lead to an increase in the friction coefficient, resulting in a damping ratio greater than that of the internal oscillator. By increasing the roughness of the contact surface between the

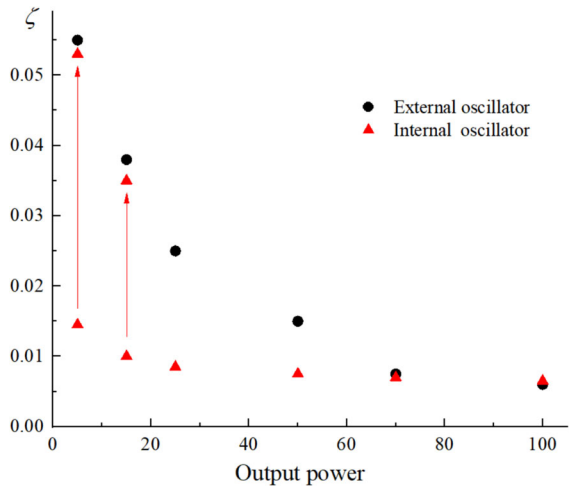

Fig. 17 Damping ratio of the external and internal oscillators with different pump output powers

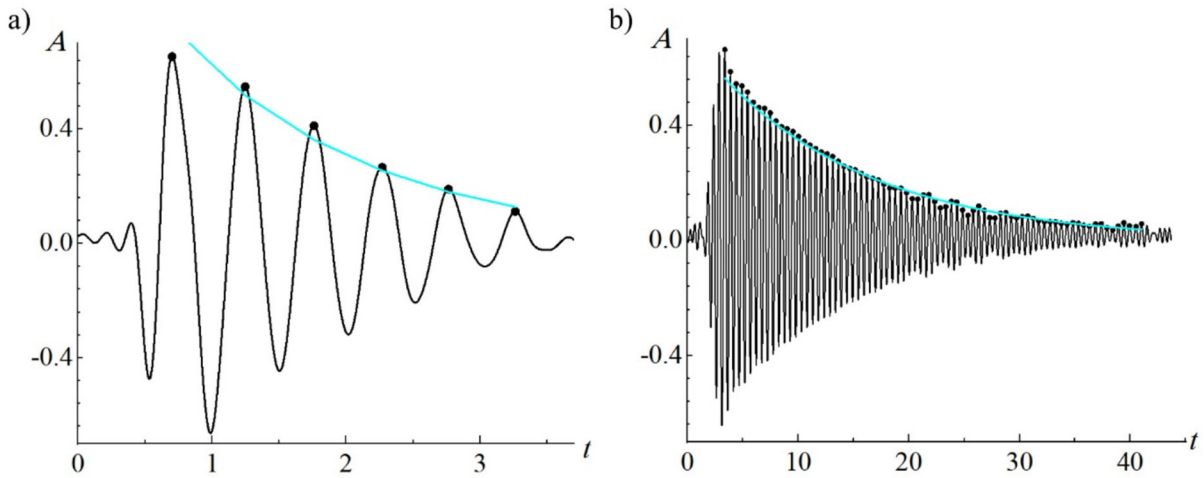

Fig. 16 The decay curves of the measured acceleration: **a** Output power of 5; **b** Output power of 100. The *x*-axis represents time [s], and the *y*-axis represents the measured acceleration amplitude [*g*]

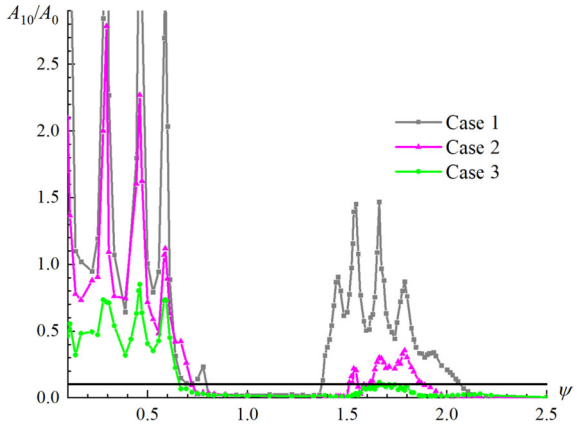

Fig. 18 Frequency–response curves for three cases with respect to the values of the damping ratio: Case 1, power of the air pump = 100; Case 2, power of the air pump = 15; Case 3, power of the air pump = 5 (The corresponding parameter values are labelled in Fig. 9c)

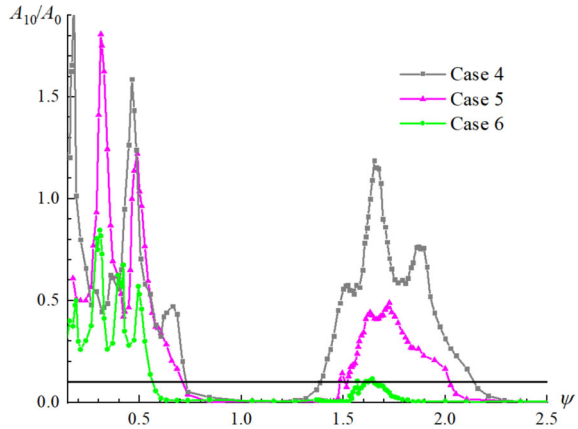

Fig. 19 Frequency–response curves for three cases with respect to the numbers of masses: Case 4, $n = 6$; Case 5, $n = 10$; Case 6, $n = 17$ (The corresponding parameter values are labelled in Fig. 9c)

internal oscillator and the track, the sliding damping of the internal oscillator can be enhanced, leading to a non-dimensional damping coefficient of $\rho \approx 1$, which matches the theoretical considerations. The relevant experimental details can be found in Appendix.

3.3 Frequency–response curves

To further validate the appearance of FinAR and SemiFinAR, Fig. 18 presents the frequency–response curves of the metastructure under three damping cases when $\mu = \kappa = \rho = 1$ and $n = 10$. The powers of the air pump for Cases 1, 2, and 3 are 100, 15, and 5, respectively. Note that these cases are also labelled in the behavioural map presented in Fig. 9c.

The results indicate that increasing the damping of the oscillators can effectively diminish the resonance amplitudes on both sides of the bandgap. However, for Case 2, the width of the bandgap remains limited, similar to the FinAR case. When the damping ratio is sufficiently high, as shown in Case 3, the response amplitude on the right side of the bandgap is further reduced to below the threshold, effectively validating the SemiFinAR case.

Furthermore, with the system's damping ratio maintained approximately constant at 0.03, Fig. 19 presents the frequency–response curves of the metastructure for the system with three different numbers of masses. The number of units for Cases 4, 5, and 6 are $n = 6$, 10 and 17, respectively (these cases are also labelled in the behavioural map presented in Fig. 9c to indicate the parameter values to which they correspond). It can be observed that as the number of units increases, the width of the stopband expands, and the FinAR case gradually evolves into the SemiFinAR case.

4 Conclusions

This study has been concerned with theoretical and experimental investigations of a longitudinally excited chain of external linear oscillators with internal linear oscillators attached to them for the sake of passive vibration control. Following den Hartog's concept, the natural frequency of internal oscillators has been tuned to the frequency of the external oscillators. The theoretical analysis of the undamped chain has confirmed that a zero-amplitude response (stopband) appears around the tuned frequency, and this has further been used as a benchmark. For a smaller number of these masses, the width of the stopband is very small, but as this number increases, until appr. 10, the width increases more rapidly, and then after app. 30 of them, its change becomes negligible, i.e. the saturation phenomenon appears. Then, a linearly viscously damped chain with external and internal oscillators has been investigated in detail. Three cases of qualitatively different vibration attenuation regions have been identified: the case of no attenuation region, a infinite vibration attenuation region (appearing

between certain frequencies) and a semi-infinite vibration attenuation region (appearing as limited on the left-hand side frequency and yielding vibration attenuation above this cut-off frequency). As far as the authors are aware, these results are novel and are of fundamental importance for vibration control. Further, to get deeper insight into such distinctive response, behavioural mapping has been done. Thus, it has been determined when, depending on the combination of the system parameter (the mass ratio, the non-dimensional damping coefficient and the number of units), each of three qualitatively different responses can take place.

The investigations carried out have yielded another novel result that the boundary between the finite and semi-infinite vibration region changes in a nonlinear way, i.e. that the non-dimensional damping coefficient and the number of units are inversely proportional with the coefficient that depends on the mass ratio. The larger the mass ratio, the smaller this coefficient. It is interesting to note that for the light subunits corresponding to the mass ratio of 10%, this coefficient is equal to unity. Another new result gained in this study regards the fact that there is a threshold of damping for which the case of a semi-infinite vibration attenuation region appears, and it depends on the number of units. This threshold decreases as the number of units increases. For a very small number of units and the range of the non-dimensional damping coefficient considered, the case of a semi-infinite vibration attenuation region can be physically unattainable. This study has also innovatively introduced and determined the critical non-dimensional damping ratio. The values of the non-dimensional damping ratio higher than this critical one, assure the appearance of the semi-infinite vibration attenuation region in the system response. Its dependence on the non-dimensional total mass has been found to be nonlinear. Another novel result obtained regards metastructures with a smaller number of units and, therefore, smaller total mass. It has been obtained that for this type of chains, there is a conservation law for the critical non-dimensional damping ratio and the minimal total mass needed, meaning that their product is constant and smaller than unity.

Theoretical findings have been checked experimentally with an original way of damping control. A metastructure has been 3D printed and placed on a triangular cross-sectional air track, which has been employed to regulate the damping ratio throughout the motion of the metastructure. An air pump has been utilised to power the air track, generating high-pressure airflow through small apertures on the surface. In this way, the air pump features an adjustable power output capability, allowing for precise control of the damping coefficient. The experiment conducted with this setup has successfully confirmed the existence of distinctive vibration attenuation regions.

Although the system considered has been linear with respect to the stiffness and damping forces, the investigations conducted revealed a nonlinear relationship between the non-dimensional damping coefficient and the number of units corresponding to the bifurcation line separating two qualitatively different responses: the finite and semi-infinite vibration region, as well as the nonlinear change of the critical non-dimensional damping ratio with the non-dimensional total mass that causes the appearance of the semi-infinite vibration attenuation region. Future research could be straightforwardly expanded to exploit nonlinearities in these two types of forces, for example a hardening/softening/bistable/power-form restoring force and/or various polynomial power-form damping forces, for the sake of widening a finite vibration attenuation region reported herein or at lowering the cut-off frequency of a semi-infinite vibration attenuation region.

Acknowledgements The first two authors acknowledge the use of the High-Performance Computing Facility, and associated support services at the Faculty of Science, University of Novi Sad, in the completion of the work whose results are presented in figures in Section 2. This paper is the result of the bilateral Serbia-China research project 'Noise and Vibration Isolation through Nonlinear Metastructures' (acronym NOLIMAST), supported by the Ministry of Science, Technological Development and Innovation of the Republic of Serbia and the National Key Research and Development Program of China under Grant No. 2021YFE0110900.

Author contributions I. Kovacic: Conceptualization, Methodologies, Theoretical analyses, Writing—review & editing. Lj. Teofanov: Numerical analysis in Wolfram

Mathematica. R. Zhu: Conceptualization of experimental methodology; X. Wang, Z. Zhao: Conducting experiments and analyses of experimental results.

Funding Ministry of Science, Technological Development and Innovation of the Republic of Serbia, NOLIMAST, NOLIMAST, National Key Research and Development Program of China, 2021YFE0110900, 2021YFE0110900, 2021YFE0110900.

Data availability No datasets were generated or analysed during the current study.

Declarations

Conflict of interest The authors declare that the research was conducted in the absence of any commercial or financial relationships that could be construed as a potential conflict of interest.

Appendix

During the damping identification experiment, tests were conducted separately for the isolated internal and external oscillators. Each oscillator was subjected to an identical initial displacement of 45 mm and then released, as shown in Fig. 20. A representative unit is selected to illustrate the influence of pump power on the damping ratio, as shown in Fig. 17. Similar phenomena were also observed in the other oscillators. Surface roughness was increased by introducing small, thin layers onto the contact surfaces of the oscillator. Specifically, the addition of localized thin layers reduces surface smoothness and introduces uneven surface thickness, thereby enhancing the overall roughness.

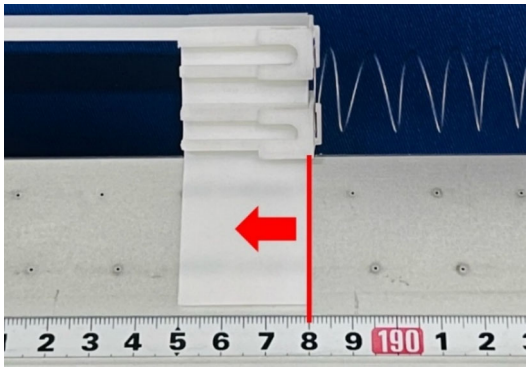

Fig. 20 The air track is marked with scales for measurements, and the initial position of the oscillator is indicated

References

1. Cambridge International Dictionary of English, 4 Edition, Cambridge University Press, Cambridge (2013)
2. https://www.encyclopedia.com/science/encyclopedias-almanacs-transcripts-and-maps/mountain-chains. (2024) Accessed 29 September 2024
3. https://www.britannica.com/science/chain-unit-of-length. (2024) Accessed 29 September 2024
4. Manevich, A.I.: The Mechanics of Nonlinear Systems with Internal Resonances Preface and Contents. Imperial College Press, London (2020)
5. Stefanovska, A., McClintock, P. (eds.): The Physics of Biological Oscillators. Springer, Cham (2021)
6. Den Hartog, J.P.: Mechanical Vibrations. McGraw-Hill, New York (1934) (reprinted by Dover, 1985)
7. Fermi, E., Pasta, J., Ulam, S.: Studies of Nonlinear Problems. Los Alamos report LA-1940, (1955)
8. Sun, J.Q., Jolly, M., Norris, M.A.: Passive, adaptive and active tuned vibration absorbers—A survey. J. Vib. Acoust. **117**(B), 234–242 (1995)
9. Haddow, A., Shaw, S.W.: Centrifugal pendulum vibration absorbers: an experimental and theoretical investigation. Nonlinear Dyn. **34**, 293–307 (2003)
10. Kela, L., Vähäoja, P.: Recent studies of adaptive tuned vibration absorbers/neutralizers. Appl. Mech. Rev. **62**, 1–9 (2009)
11. Huang, X.B., Yang, B.T.: Towards novel energy shunt inspired vibration suppression techniques: Principles, designs and applications. Mecha. Syst. Signal Process **182**, 109496 (2023)
12. Hussein, M.I., Leamy, M.J., Ruzzene, M.: Dynamics of phononic materials and structures: historical origins, recent progress, and future outlook. Appl. Mech. Rev. **66**, 040802 (2014)
13. Ji, J.C., Luo, Q.T., Ye, K.: Vibration control based metamaterials and origami structures: a state-of-the-art review. Mech. Syst. Signal Process. **161**, 107945 (2021)
14. Liu, Z., Zhang, X., Mao, Y., Zhu, Y.Y., Yang, Z., Chan, C.T., Sheng, P.: Locally resonant sonic materials. Science **289**, 1734–1736 (2000)
15. Wang, G., Wen, X., Wen, J.H., Liu, Y.Z.: Quasi-one-dimensional periodic structure with locally resonant band gap. J. Appl. Mech. **73**, 167–170 (2006)
16. Huang, H.H., Sun, C.T.: Wave attenuation mechanism in an acoustic metamaterial with negative effective mass density. New J. Phys. **11**, 013003 (2009)
17. Huang, H.H., Sun, C.T., Huang, G.L.: On the negative effective mass density in acoustic metamaterials. Int. J. Eng. Sci. **47**, 610–617 (2009)
18. Xiao, Y., Wen, J.H., Wen, X.S.: Longitudinal wave band gaps in metamaterial-based elastic rods containing multi-degree-of-freedom resonators. New J. Phys. **14**, 033042 (2012)
19. Nobrega, E.D., Gautier, F., Pelat, A., Dos Santos, J.M.C.: Vibration band gaps for elastic metamaterial rods using wave finite element method. Mech. Syst. Signal Process. **79**, 192–202 (2016)
20. Frank Pai, P.: Metamaterial-based broadband elastic wave absorber. J. Intell. Mater. Syst. Struct. **21**, 517–528 (2010)

21. Lee, S., Ahn, C.H., Lee, J.W.: Vibro-acoustic metamaterial for longitudinal vibration suppression in a low frequency range. Int. J. Mech. Sci. **144**, 223–234 (2018)
22. Hobeck, J.D., Laurent, C.M.V., Inman D.J.: 3D printing of metastructures for passive broadband vibration suppression. In: 20th International Conference on Composite Materials Copenhagen, pp. 1–9 (2015).
23. Reichl, K.K., Inman, D.J.: Lumped mass model of a 1D metastructure for vibration suppression with no additional mass. J. Sound Vib. **403**, 75–89 (2017)
24. Kovacic, I., Rakaric, Z., Kanovic, Z., Rajs, V.: Metastructure with integrated oscillators of constant, linearly and nonlinearly varying natural frequency. Front. Phys. **10**, 934998 (2022)
25. Kovacic, I., Radomirovic, D.: Mechanical Vibrations: Fundamentals with Solved Examples. John Willey & Sons, Hoboken (2017)
26. Rivin, E.: Stiffness and Damping in Mechanical Design. CRC Press, Boca Raton (1999)